Maturation of ureter-bladder connection in mice is controlled by LAR family receptor protein tyrosine phosphatases

Noriko Uetani,[1] Kristen Bertozzi,[1] Melanie J. Chagnon,[1] Wiljan Hendriks,[2] Michel L. Tremblay,[1] and Maxime Bouchard[1]

[1]Goodman Cancer Centre, Department of Biochemistry, McGill University, Montreal, Quebec, Canada. [2]Department of Cell Biology, Radboud University Nijmegen Medical Centre, Nijmegen, The Netherlands.

Congenital anomalies affecting the ureter-bladder junction are frequent in newborns and are often associated with other developmental defects. However, the molecular and morphological processes underlying these malformations are still poorly defined. In this study, we identified the leukocyte antigen–related (LAR) family protein tyrosine phosphatase, receptor type, S and F (Ptprs and Ptprf [also known as Lar], respectively), as crucially important for distal ureter maturation and craniofacial morphogenesis in the mouse. Embryos lacking both *Ptprs* and *Ptprf* displayed severe urogenital malformations, characterized by hydroureter and ureterocele, and craniofacial defects such as cleft palate, micrognathia, and exencephaly. The detailed analysis of distal ureter maturation, the process by which the ureter is displaced toward its final position in the bladder wall, leads us to propose a revised model of ureter maturation in normal embryos. This process was deficient in embryos lacking *Ptprs* and *Ptprf* as a result of a marked reduction in intrinsic programmed cell death, thereby causing urogenital system malformations. In cell culture, Ptprs bound and negatively regulated the phosphorylation and signaling of the Ret receptor tyrosine kinase, whereas Ptprs-induced apoptosis was inhibited by Ret expression. Together, these results suggest that ureter positioning is controlled by the opposing actions of Ret and LAR family phosphatases regulating apoptosis-mediated tissue morphogenesis.

Introduction

Congenital anomalies of the kidney and urinary tract (CAKUT) are among the most common birth defects found in human infants (1 in 500 live births) (1). CAKUT comprise a number of developmental anomalies at the level of the kidney (e.g., hydronephrosis, hypoplasia, adysplasia, duplex kidney), ureter (e.g., severe dilation of the ureter [hydroureter]), and bladder (e.g., ectopic ureteral orifice, fluid-filled cyst [ureterocele]). These anomalies often lead to severe kidney dysfunction and a potentially lethal condition requiring kidney transplant. Despite the large spectrum of disorders associated with CAKUT, most of these malformations result from a failure to properly position the ureter within the bladder wall (2, 3). Yet, relatively little is known about the morphological, cellular, and molecular aspects underlying ureter-bladder connection.

In mice, urogenital system development is initiated with the formation of the nephric duct in the intermediate mesoderm on E8.5 of development. The newly formed nephric duct progresses caudally to join the cloaca (bladder/urethra/rectum primordium). At E10.5, the metanephric mesenchyme, located at the level of the hindlimbs, induces the formation of the ureteric bud, a diverticulum of the nephric duct that invades the metanephric mesenchyme to form the ureter and collecting system of the definitive kidney. For the ureter to be functional, its distal connection point must be displaced from the nephric duct to the bladder prior to the onset of urine flow from the kidney. According to a model first proposed by Mackie and Stephens (2), the site of ureter budding along the nephric duct has a key influence on the final positioning of the ureter within the bladder wall (reviewed in ref. 4). A caudal budding of the ureter would indeed place the ureter/bladder (vesicoureteral) junction too high in the bladder wall, resulting in vesicoureteral reflux. Such a defect is observed in *Pax2*$^{+/-}$ mouse embryos (5). On the other hand, an ectopic rostral budding site prevents the ureter from reaching the bladder, leading to hydroureter and hydronephrosis as a result of vesicoureteral junction obstruction (VUJO) of the ectopic ureter. Several mouse models have been described with such malformations (6–9). An alternative cause for VUJO is a defect in the process of distal ureter maturation following a normal budding of the ureter. Indeed, recent data suggest that reduced apoptosis in the common nephric duct (CND) (located between the ureter-nephric duct branch point and the cloaca) could delay distal ureter maturation, leading to urinary tract malformations (10). In such cases, embryos are characterized by hydroureter/hydronephrosis associated with a single ureter.

Among the most important regulators of urinary tract morphogenesis are components of the Ret tyrosine kinase signaling pathways (11). This pathway is central to ureter induction and subsequent kidney growth as well as for distal ureter maturation (12). Activation of the Ret–glial cell derived neurotrophic factor (GDNF) family receptor α1 (Ret-GFRα1) receptor complex by the GDNF ligand results in tyrosine phosphorylation of Ret, which provides phospho-tyrosine (pY) docking sites for adaptor or effector proteins such as PLCγ (at pY1015) and Shc, IRS1/2, DOK1/4/5/6, FRS2, PKCα, Shank3, and Enigma (at pY1062) (13). Recent mouse genetic studies revealed that these 2 phospho-tyrosines are the most critical for urinary tract development (14–16).

Conflict of interest: The authors have declared that no conflict of interest exists.

Nonstandard abbreviations used: CAKUT, congenital anomalies of the kidney and urinary tract; CND, common nephric duct; GDNF, glial cell derived neurotrophic factor; GFRα1, GDNF family receptor α1; LAR, leukocyte antigen–related; Ptprs, protein tyrosine phosphatase, receptor type, S; RPTP, receptor protein tyrosine phosphatase; VUJO, vesicoureteral junction obstruction.

Citation for this article: *J. Clin. Invest.* **119**:924–935 (2009). doi:10.1172/JCI37196.

Table 1
Survival and frequency of malformations in *Ptprs;Ptprf* allelic series

Genotype		Predicted	Observed ratio (%)		Urinary tract malformations[A]		Craniofacial malformations[A]		
Ptprs	*Ptprf*	ratio (%)	E18.5	4 weeks	Hydroureter	Duplex-system	Micrognathia	Exencephaly	Open eye
+/+	+/+	6.25	5.66	9.33	0% (0/14)	0% (0/14)	0% (0/14)	0% (0/14)	0% (0/14)
+/+	+/ΔP	12.50	12.58	15.67	0% (0/29)	0% (0/29)	0% (0/29)	0% (0/29)	0% (0/29)
+/+	ΔP/ΔP	6.25	7.55	6.33	2% (1/42)	0% (0/42)	0% (0/42)	0% (0/42)	0% (0/42)
+/–	+/+	12.50	10.06	16.67	0% (0/21)	5% (1/21)	0% (0/21)	5% (1/21)	0% (0/21)
+/–	+/ΔP	25.00	23.27	36.00	0% (0/43)	2% (1/43)	2% (1/43)	2% (1/43)	0% (0/43)
+/–	ΔP/ΔP	12.50	16.35	12.33	0% (0/41)	0% (0/41)	7% (3/41)	0% (0/41)	0% (0/41)
–/–	+/+	6.25	6.92	2.00	0% (0/13)	0% (0/13)	0% (0/13)	0% (0/13)	0% (0/13)
–/–	+/ΔP	12.50	11.95	1.67	4% (1/26)	0% (0/26)	0% (0/26)	0% (0/26)	0% (0/26)
–/–	ΔP/ΔP	6.25	5.66	0.00	52% (16/31)[B]	13% (4/31)	45% (14/31)	23% (7/31)	23% (7/31)
Total			*n* = 159	*n* = 300					

[A]Shown in parentheses is the number of animals showing phenotype at E18.5/number of animals analyzed. [B]Includes duplex-system phenotype.

Importantly, phospho-tyrosine–dependent signaling is reversibly regulated by members of the protein tyrosine phosphatase family. Among these enzymes, the leukocyte antigen–related (LAR) receptor protein tyrosine phosphatase (RPTP) subfamily plays an important role during embryonic development and adult life. This subfamily is composed of 3 highly related enzymes, namely LAR, RPTPσ, and RPTPδ (encoded by the genes protein tyrosine phosphatase, receptor type, F [*Ptprf*], *Ptprs*, and *Ptprd*, respectively) (17), which show unique as well as redundant activities (18–26). LAR is necessary for normal brain and mammary gland development (23–26), while RPTPσ is important for pituitary development, glucose homeostasis, and nerve regeneration (19–22). Interestingly, LAR is able to counteract the oncogenic activity of an activated form of RET (MEN2A) (27). In spite of the fact that both RPTPs are expressed in the developing urogenital system, no role has yet been found for them in this embryonic structure.

In this study, we identified 2 members of the LAR-RPTPs, RPTPσ and LAR, as key modulators of distal ureter maturation and craniofacial development. *Ptprs;Ptprf* double-mutant embryos exhibited craniofacial malformations such as cleft palate, small lower jaw (micrognathia), and eye dysplasia, while urinary tract anomalies were characterized by hydronephrosis, hydroureter, duplex system, and ureterocele. We show that the absence of RPTPσ and LAR phosphatase activity prevents the normal execution of the apoptotic program necessary for CND regression, resulting in inappropriate tissue survival and delayed distal ureter maturation. Moreover, we demonstrate that Ret expression can suppress RPTPσ-induced apoptotic cell death, while RPTPσ directly binds to Ret and modulates GDNF-Ret signaling. Taken together, our results reveal what we believe are new and crucial morphogenetic functions performed in concert by RPTPσ and LAR during embryonic development.

Results

Ptprs;Ptprf double-mutant embryos show severe craniofacial and urinary tract anomalies. To determine the function of RPTPσ and LAR in the urogenital system and other tissues, we generated an allelic series including both gene mutations. *Ptprs* inactivation results in a complete absence of gene product (19), while *Ptprf* mutation generates in a truncated transcript lacking the phosphatase domain ($Ptprf^{\Delta P}$) (23). We initially determined the viability of these mice at E18.5 (the day before birth) and at 4 weeks of age. At E18.5, all allelic combinations showed the expected Mendelian ratios, excluding embryonic lethality for any *Ptprs;Ptprf* mutant embryos. At 4 weeks of age, the loss of RPTPσ led to a reduction in the number of viable mice, in accordance with previous observations (19). Noticeably, only $Ptprs^{-/-}Ptprf^{\Delta P/\Delta P}$ animals were never found at this age, indicating that together RPTPσ and LAR are necessary for postnatal survival (Table 1).

A gross morphological analysis of *Ptprs;Ptprf* allelic series at E18.5, revealed no significant differences in body weight between control (1.18 g ± 0.10 SD, *n* = 41) and $Ptprs^{-/-}Ptprf^{\Delta P/\Delta P}$ (1.13 g ± 0.09 SD, *n* = 13). However, this analysis revealed a number of craniofacial and urogenital malformations specific to $Ptprs^{-/-}Ptprf^{\Delta P/\Delta P}$ embryos. The craniofacial defects consisted of exencephaly, micrognathia, and a failure in eyelid closure (Figure 1, A–C). The histological analysis of $Ptprs^{-/-}Ptprf^{\Delta P/\Delta P}$ heads additionally revealed the presence of cleft palate (Figures 1, D and E) and malformations of the eye, including hyperplastic inner nuclear layers (primitive ganglion cells) and persistence of prominent hyaloid arteries with abnormal retrolental tissues (Figure 1, F–I). In addition, $Ptprs^{-/-}Ptprf^{\Delta P/\Delta P}$ embryos had a disorganized neural retina (Figure 1I). A quantification of the gross morphological defects revealed an incomplete penetrance of the phenotypes, with micrognathia being observed in 45% of embryos (14/31), while exencephaly and opened eyelids were each seen in 23% of embryos (7/31) (Table 1). Some of these malformations were also observed at a low frequency in other allelic combinations, suggesting a dosage effect of RPTPσ and LAR.

In addition to these craniofacial defects, $Ptprs^{-/-}Ptprf^{\Delta P/\Delta P}$ embryos harbored striking abnormalities of the urinary tract such as hydroureters, hydronephrosis, and duplicated ureter/renal systems (Figure 2, A–C). The quantification of these anomalies revealed a frequency of 52% of embryos (16/31) with severe uni- or bilateral hydroureters/hydronephrosis (Table 1). Interestingly, 75% of those embryos (12/16) harbored a single ureter and renal system, while only 25% (4/16) had a duplicated ureter and renal system. A number of additional milder cases not recorded as hydroureter appeared to have a single dilated ureter (indicated by an arrowhead in Figure 2B). The analysis of $Ptprs^{-/-}Ptprf^{\Delta P/\Delta P}$ kidneys by tissue histopathology revealed a dilation of the renal pelvis with secondary atrophy of the surrounding renal parenchyma in cases with hydroureter/hydronephrosis, while the remaining double-mutant kidneys looked normal in appearance, indicating that RPTPσ and

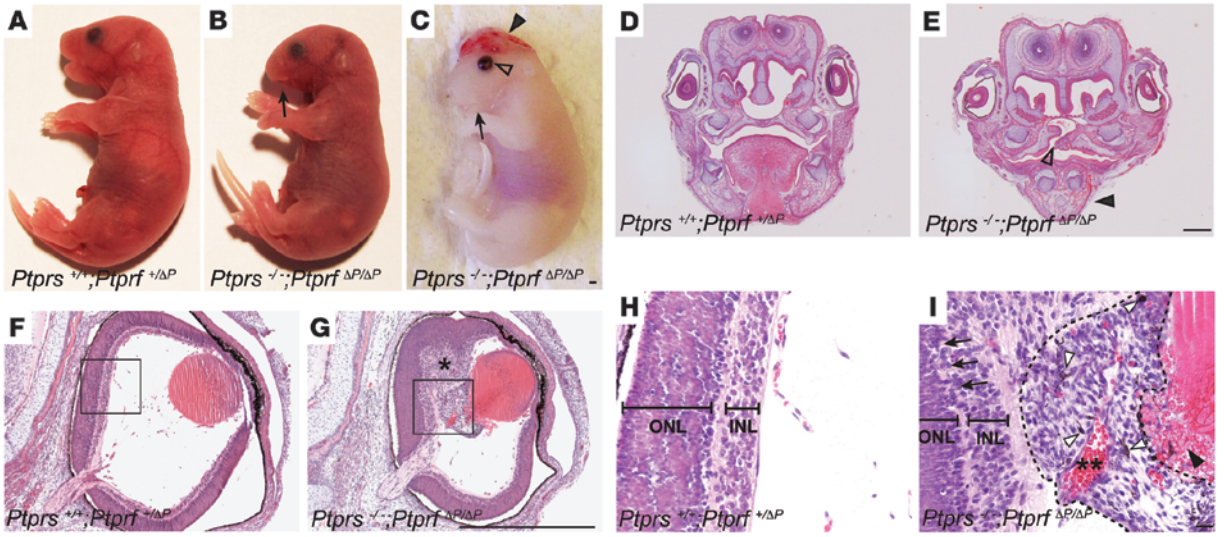

Figure 1
Craniofacial anomalies in *Ptprs;Ptprf* double-mutant embryos. (**A**–**C**) Gross morphological appearance of control (**A**) and *Ptprs*$^{-/-}$*Ptprf*$^{\Delta P/\Delta P}$ (**B** and **C**) embryos at E18.5. Note the presence of micrognathia (arrow), exencephaly (arrowhead) and open eyelid (open arrowhead) in *Ptprs*$^{-/-}$*Ptprf*$^{\Delta P/\Delta P}$ embryos. (**D** and **E**) Coronal sections of the face region of control (**D**) and *Ptprs*$^{-/-}$*Ptprf*$^{\Delta P/\Delta P}$ (**E**) embryos stained by H&E. The tongue and palate of control embryos were readily distinguishable, whereas *Ptprs*$^{-/-}$*Ptprf*$^{\Delta P/\Delta P}$ embryos showed smaller lower jaw (arrowhead) and an opened palate (open arrowhead) at an equivalent level of the head. (**F**–**I**) Coronal sections of the eye of control (**F** and **H**) and *Ptprs*$^{-/-}$*Ptprf*$^{\Delta P/\Delta P}$ (**G** and **I**) embryos stained by H&E. In contrast to the characteristic eye morphology observed in control embryos, *Ptprs*$^{-/-}$*Ptprf*$^{\Delta P/\Delta P}$ eyes sometimes showed a hyperplastic inner nuclear layer (single asterisk in **G**) and abnormal retrolental tissue (indicated by dotted line in **I**) filling the hyaloid cavity. (**H** and **I**) High-magnification views of the boxes in **F** and **G**. (**I**) In *Ptprs*$^{-/-}$*Ptprf*$^{\Delta P/\Delta P}$ embryos, neuroretinal lamination was disorganized (arrows). Note the presence of pigmented cells (white arrowheads), the hyaloid artery within the retrolental tissue (double asterisk), and the lens degradation (black arrowhead). Scale bars: 1 mm (**A**–**G**) and 10 μm (**H** and **I**). ONL, outer nuclear layer; INL, inner nuclear layer.

LAR do not play a critical role in metanephric kidney development (data not shown). Interestingly, the presence of craniofacial defects was not correlated with the urogenital malformations.

We then focused on the morphological and molecular origin of the urinary tract malformations. Upon examination of the vesicoureteral junction of severe hydroureter/hydronephrosis cases, we observed the presence of ureterocele within the bladder, ipsilateral to the enlarged ureter and kidneys (n = 6) (Figure 2, D–G). In addition, cases of milder ureter dilation were examined at the level of the vesicoureteral junction using serial histological sections. These analyses revealed that the ureters were connected to the bladder

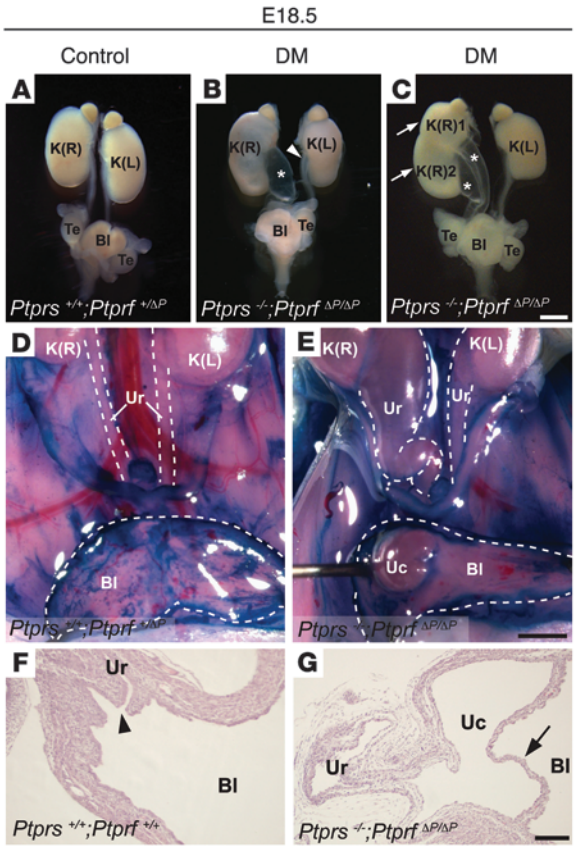

Figure 2
Urogenital system anomalies in *Ptprs;Ptprf* double-mutant embryos. (**A**–**C**) Urogenital systems dissected from E18.5 embryos. (**A**) Normal control urogenital system. (**B**) *Ptprs*$^{-/-}$*Ptprf*$^{\Delta P/\Delta P}$ urogenital system showing severe hydroureter on the right side (asterisk) and mild hydroureter on the left side (arrowhead). (**C**) *Ptprs*$^{-/-}$*Ptprf*$^{\Delta P/\Delta P}$ urogenital system harboring duplex-kidney (arrows) and duplex-hydroureter (asterisks). (**D** and **E**) Ventral views of the abdominal cavity at E18.5. Kidneys, ureters, and bladders were exposed and contrasted with methylene blue. Bladders were cut at midline and opened. Dotted lines outline the structures. (**D**) Normal control embryo. (**E**) *Ptprs*$^{-/-}$*Ptprf*$^{\Delta P/\Delta P}$ embryo showing unilateral hydroureter with ureterocele. (**F** and **G**) H&E-stained sagittal sections of bladders at the level of the vesicoureteral junction at E18.5. (**F**) Normal control. Arrowhead indicates the ureter orifice. (**G**) *Ptprs*$^{-/-}$*Ptprf*$^{\Delta P/\Delta P}$ embryo showing ureterocele membrane (arrow). Scale bars: 1 mm (**A**–**E**), 100 μm (**F** and **G**). DM, *Ptprs;Ptprf* double-mutant; K(R), right kidney; K(L), left kidney; Bl, bladder; Te, testis; Uc, ureterocele; Ur, ureter.

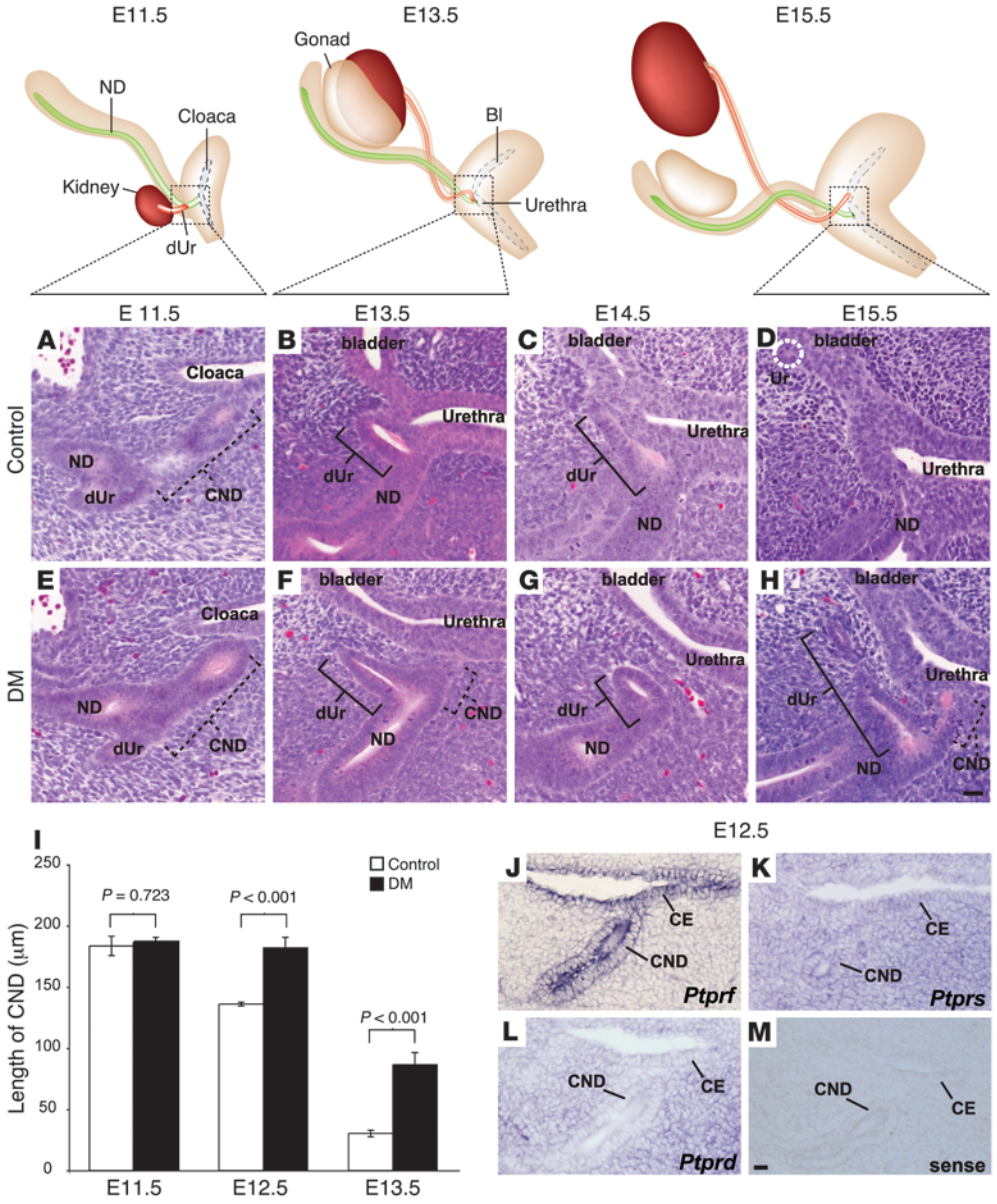

Figure 3

Distal ureter maturation defects in *Ptprs*$^{-/-}$*Ptprf*$^{\Delta P/\Delta P}$ embryos. Top: Diagrams of WT E11.5–E15.5 urogenital systems. (**A**–**H**) H&E-stained sagittal sections of representative control (**A**–**D**) and *Ptprs*$^{-/-}$*Ptprf*$^{\Delta P/\Delta P}$ urogenital systems (**E**–**H**) at different developmental stages. At E11.5, no difference in CND length was observed between control (**A**) and *Ptprs*$^{-/-}$*Ptprf*$^{\Delta P/\Delta P}$ embryos (**E**). CND length is indicated by dotted lines, distal ureter is indicated by solid lines. At E13.5 (**B** and **F**) and E14.5 (**C** and **G**), the distal ureter was in close apposition with the bladder epithelium in control embryos (**B** and **C**). In contrast, *Ptprs*$^{-/-}$*Ptprf*$^{\Delta P/\Delta P}$ embryos harbored a distal ureter located away from the bladder (**F** and **G**). (**D** and **H**) At E15.5, distal ureter elimination allowed the ureter to reconnect into bladder (dotted white circle) in a normal control (**D**), while the distal ureter remained at a distance from the bladder epithelium in *Ptprs*$^{-/-}$*Ptprf*$^{\Delta P/\Delta P}$ embryos (**H**). (**I**) Length of CNDs was quantified at different developmental stages. Although there was no difference in CND lengths at E11.5, the CND was significantly longer in *Ptprs*$^{-/-}$*Ptprf*$^{\Delta P/\Delta P}$ at E12.5 and E13.5. Error bars indicate SEM. (**J**–**M**) In situ hybridization on E12.5 transversal sections using antisense cRNA probes against *Ptprf* (**J**), *Ptprs* (**K**), *Ptprd* (**L**), and a sense probe against *Ptprs* (**M**). (**J**) *Ptprf* expression was mostly restricted to the CND, while *Ptprs* expression was detected ubiquitously in the mesenchyme and cloaca epithelium (**K**). (**L**) *Ptprd* was predominantly expressed in the mesenchyme. (**M**) A sense *Ptprs* probe was used as negative control. Scale bars: 10 μm. ND, nephric duct; dUr, distal ureter; CE, cloaca epithelium.

but winding abnormally, proximal to the connection point (Supplemental Figure 1; supplemental material available online with this article; doi:10.1172/JCI37196DS1). Together, these results identify craniofacial and urogenital system morphogenesis as 2 crucial sites of LAR-RPTP activity. In the urogenital system, the data further indicated that hydroureter and hydronephrosis developed as a result of an obstruction at the vesicoureteral junction, leading to ureterocele in *Ptprs*$^{-/-}$*Ptprf*$^{\Delta P/\Delta P}$ embryos.

Impaired CND elimination in Ptprs;Ptprf double-mutant embryos. Several possibilities could explain the vesicoureteral obstruction observed in *Ptprs*$^{-/-}$*Ptprf*$^{\Delta P/\Delta P}$ mouse embryos. The most immediate explanation would be that the ureter forms at a position more rostral than normal. Alternatively, the obstruction may come as a result of bladder primordium hyperplasia or be due to a defect in distal ureter maturation. To examine these possibilities in detail, we first monitored the morphological events of ureter maturation in normal embryos. To obtain a sufficient resolution, we performed this analysis on serial sections revealed by H&E staining at different stages of development. At E11.5, the CND was visualized between the distal ureter and the cloaca (Figure 3A). By E13.5, the CND had almost completely disappeared, bringing the distal ureter in the vicinity of the bladder/urethra epithelium (Figure 3B). Unexpectedly, we found that the distal ureter subsequently lay down on the bladder/urethra epithelium and was also eliminated (Figure 3, C and D). This led to the generation of a new ureter connection point at the level of the bladder primordium, while the nephric duct remained connected at the level of the urethra primordium (Figure 3D).

We next examined these morphological rearrangements in

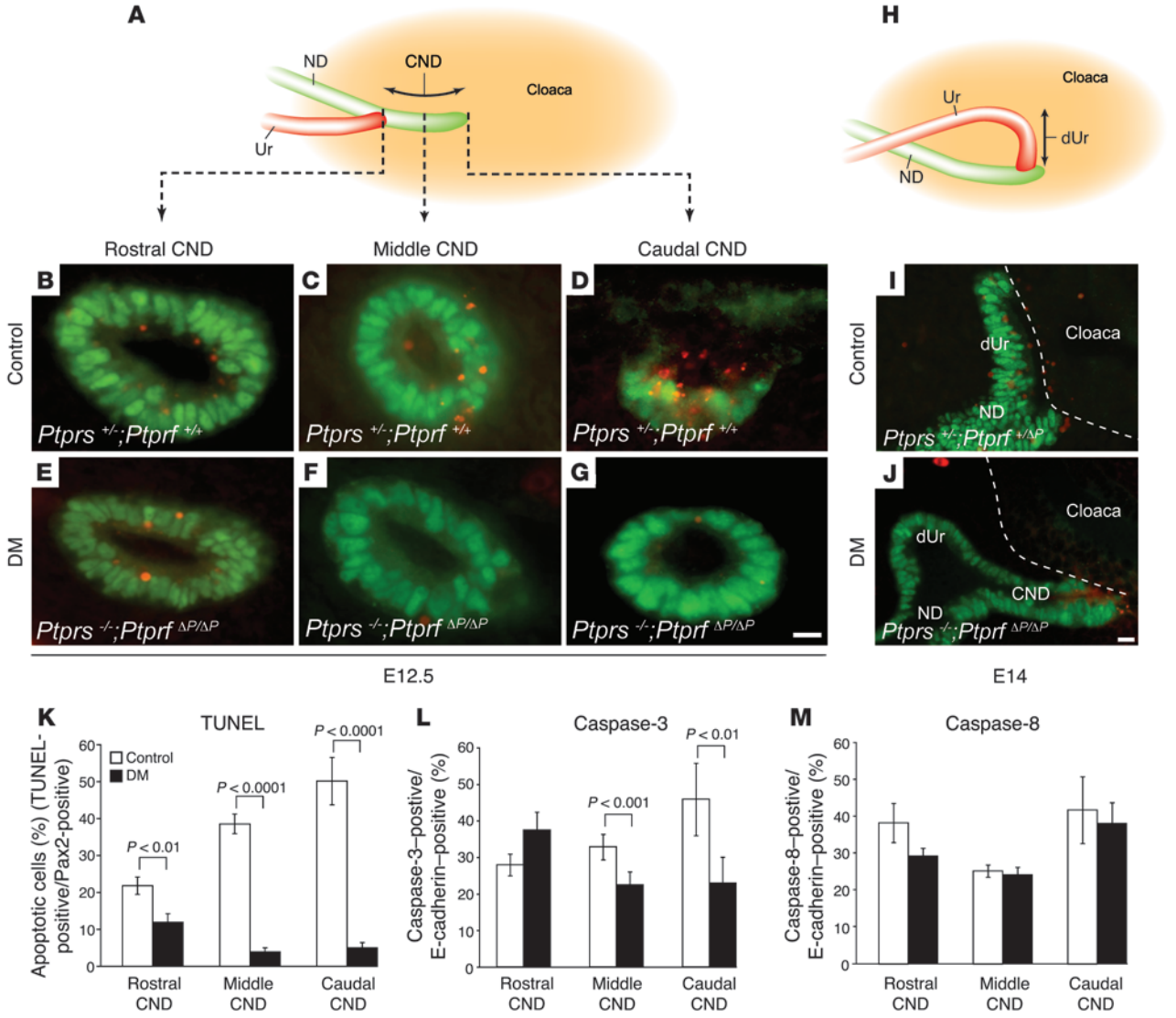

Figure 4

Apoptotic cell death in CND. (**A**) Schematic representation of sagittal view of a urogenital system at E12.5. Dotted lines indicate the position of sections shown in **B**–**G**. (**B**–**G**) TUNEL stain (red) and anti-Pax2 counterstain (green) on transverse sections of E12.5 embryos derived from control (**B**–**D**) and *Ptprs*$^{-/-}$*Ptprf*$^{\Delta P/\Delta P}$ embryos (**E**–**G**). CNDs were separated into 3 sections: rostral CND (closest to ureter), middle CND, and caudal CND (closest to bladder). (**H**) Schematic representation of sagittal view of normal urogenital system at E14.0. (**I** and **J**) TUNEL stain (red) and anti-Pax2 counterstain (green) on sagittal sections of E14.0 control (**I**) and *Ptprs*$^{-/-}$*Ptprf*$^{\Delta P/\Delta P}$ (**J**) urogenital systems. Dotted lines outline the cloaca epithelium. (**K**–**M**) Quantitative analysis of the cell death observed in control and *Ptprs*$^{-/-}$*Ptprf*$^{\Delta P/\Delta P}$ CNDs. (**K**) Control embryos showed a strong increase in apoptosis along the rostrocaudal axis of the CND (TUNEL-positive/Pax-2–positive; $n = 8$ CNDs). In contrast, *Ptprs*$^{-/-}$*Ptprf*$^{\Delta P/\Delta P}$ embryos showed a reduction in apoptotic cell death ($n = 8$ CNDs). (**L**) Quantitative analysis of caspase-3–positive cells showed a reduction in activated caspase-3–positive signals in the middle and caudal CND of *Ptprs*$^{-/-}$*Ptprf*$^{\Delta P/\Delta P}$ embryos ($n = 4$ CNDs for each genotype). (**M**) Quantitative analysis of activated caspase-8–positive cells. No significant difference was detected between control and *Ptprs*$^{-/-}$*Ptprf*$^{\Delta P/\Delta P}$ embryos ($n = 6$ CNDs for each genotype). Scale bars: 10 μm. The results shown are means ± SD.

Ptprs;Ptprf double-mutant mouse embryos. At E11.5, the CND of control and mutant embryos had a similar morphology and length (control, 183.6 ± 15.7 μm SD, $n = 3$ embryos; *Ptprs;Ptprf* double-mutant, 186.8 ± 7.4 μm SD, $n = 3$ embryos) (Figure 3, A, E, and I). The ureter budding site was therefore not affected in mutant embryos harboring a single ureter. By E13.5, when the CND had essentially been eliminated in control embryos, we could still detect the distal ureter running through the bladder/urethra mesenchyme, while the CND was still clearly present (control, 30.3 ± 3.9 μm SD, $n = 3$ embryos; *Ptprs;Ptprf* double-mutant, 86.3 ± 14.2 μm SD, $n = 3$ embryos; $P < 0.001$) (Figure 3, B, F, and I). This difference in length was already significant at E12.5 with 136.0 ± 3.6 μm SD in control embryos ($n = 3$ embryos) and 182.0 ± 12.1 μm SD in *Ptprs;Ptprf* double-mutant embryos ($n = 4$ embryos; $P < 0.001$) (Figure 3I). Later-stage embryos confirmed the strong delay in CND elimination in *Ptprs;Ptprf* double-mutant embryos, since the distal ureter was still detectable in

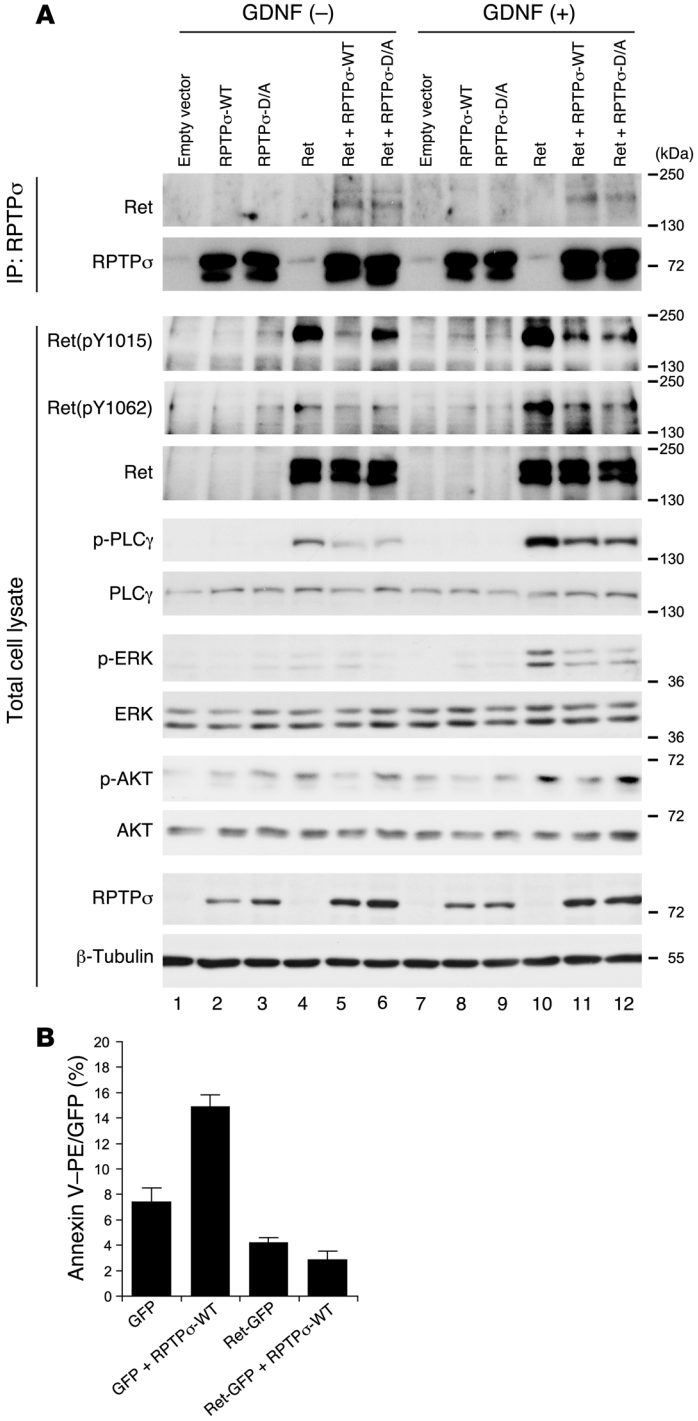

Figure 5
Molecular interaction between RPTPσ and Ret. (**A**) RPTPσ and Ret expression vectors were cotransfected in HEK293T cells and treated with or without GDNF/GFRα1. Top: Cell lysates were immunoprecipitated with anti-RPTPσ antibodies and resolved by SDS-PAGE, followed by immunoblotting with an anti-Ret antibody. The same membrane was re-blotted with anti-RPTPσ antibody. Ret proteins were specifically co-immunoprecipitated with RPTPσ-WT and RPTPσ-D/A. Bottom: Total cell lysates were immunoblotted with the indicated antibodies. Phosphorylation levels of Ret and its downstream signaling components were significantly reduced when Ret was cotransfected with RPTPσ-WT or RPTPσ-D/A. (**B**) Flow cytometric analysis of annexin V–PE staining. Cells were sorted for GFP-positive signaling. The percentage of annexin V–PE–positive cells was increased in RPTPσ-WT. This effect was suppressed by Ret coexpression. The results shown are means ± SD from 3 independent experiments.

these embryos at E14.5 and E15.5 (Figure 3, G and H) but was being eliminated and had reconnected at these stages in control embryos (Figure 3, C and D). Importantly, the ureter maturation delay was observed in all embryos examined between E12.5 and E15.5 ($n = 12$). In contrast, these analyses failed to reveal any defect at the level of the bladder or urethra primordia (Figure 3 and data not shown). From these results, we therefore concluded that distal ureter maturation is the key defective process in *Ptprs;Ptprf* double-mutant embryos.

Ptprs and Ptprf are both expressed in CND epithelium. The severe abnormalities observed at the level of the distal ureter prompted us to determine exactly where *Ptprs* and *Ptprf* were expressed in this region. To have a more comprehensive understanding of the status of RPTP expression in this tissue, we also analyzed the third subfamily member, *Ptprd*. We thus performed in situ hybridization on E12.5 mouse embryo sections using cRNA probes against *Ptprs*, *Ptprf*, and *Ptprd*. Of the 3 genes, only *Ptprf* showed an expression pattern restricted to the CND and cloaca epithelial compartments (Figure 3J). The expression of *Ptprs* was also detected in these cell types but was additionally present at similar levels in the mesenchyme surrounding the epithelial compartments (Figure 3K). However, *Ptprd* was most highly expressed in the cloaca mesenchyme, while relatively low levels of expression were detected in the CND and cloaca epithelium (Figure 3L). These results suggest that RPTPσ and LAR likely exert their redundant activity in the epithelial compartment.

CND apoptotic cell death is suppressed in Ptprs;Ptprf double-mutant embryos. To determine the cause of CND maintenance observed in $Ptprs^{-/-}Ptprf^{\Delta P/\Delta P}$ mouse embryos, we first assessed apoptotic cell death by TUNEL assay on E12.5 embryos. Epithelium-specific apoptotic signals were identified by costaining with an anti-Pax2 antibody. At this crucial stage of CND elimination, we observed a sharp apoptotic gradient along the rostrocaudal axis of the CND in control embryos (Figure 4, B–D and K). The rostral segment (at the level of the ureter) showed 22% epithelial cell death, whereas the caudal segment (located next to the cloaca epithelium) harbored about 51% of TUNEL-positive epithelial cells. In striking contrast, this apoptotic gradient was completely abolished in $Ptprs^{-/-}Ptprf^{\Delta P/\Delta P}$ embryos. Although still detectable, apoptotic cell death decreased to 12% in the rostral segment ($P < 0.01$) and was detected in less than 6% of cells in the middle and caudal segments ($P < 0.0001$) (Figure 4, E–G and K). TUNEL analysis at E14 confirmed the maintenance of apoptosis-deficient CND in $Ptprs^{-/-}Ptprf^{\Delta P/\Delta P}$ embryos and further showed the lack of apoptosis in the distal ureter segment located at a distance from the cloaca epithelium (Figure 4J). At this stage, the distal ureter was being eliminated by apoptotic cell death in control embryos (Figure 4I).

As the apoptotic CND gradient may be interpreted as a response to extrinsic rather than intrinsic apoptotic signals (28), we further investigated the underlying cell death mechanism by quantification of CND cells positive for activated caspase-3 (common to both pathways) and caspase-8 (extrinsic specific) in

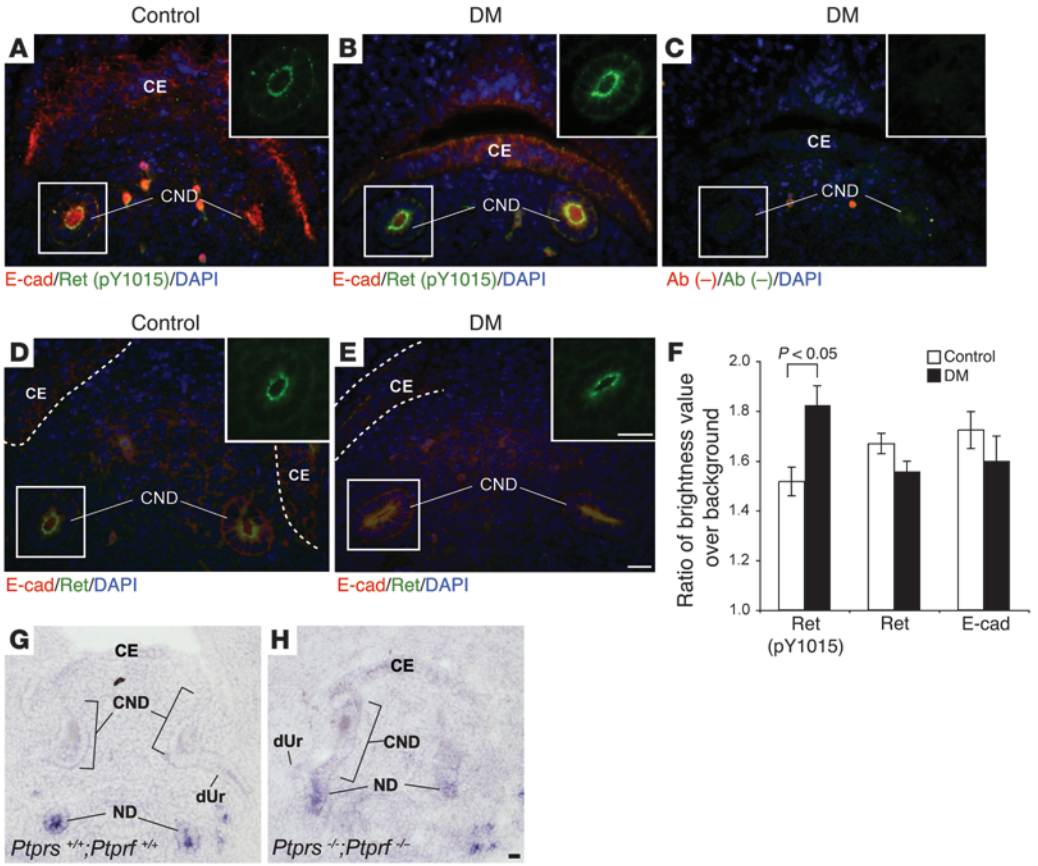

Figure 6
Immunohistochemical analysis on Ret phosphorylation. (**A**–**E**) Immunohistochemical analysis of lower urinary tracts with anti–Ret (pY1015) (green) (**A** and **B**), anti-Ret (green) (**D** and **E**), anti–E-cadherin (red) (**A**, **B**, **D**, and **E**), and no primary antibodies (**C**). Nuclei are stained with DAPI (blue). Green channel images from white line squares are presented in the upper right corners. (**F**) Quantification of immunofluorescent signals in E12.5 CND. Ret (pY1015) was significantly hyperphosphorylated in *Ptprs*$^{-/-}$*Ptprf*$^{\Delta P/\Delta P}$ CNDs (**B** and **F**) in comparison with control CNDs (**A**). Note that there were no significant differences in Ret or E-cadherin expression levels between control and *Ptprs*$^{-/-}$*Ptprf*$^{\Delta P/\Delta P}$ CND (**F**). Dotted lines outline the cloaca epithelium. (**G** and **H**) In situ hybridization analysis of E12.5 transversal sections with antisense *Ret* cRNA probes. *Ret* expression was present in the nephric duct but strongly downregulated in both control (**G**) and *Ptprs*$^{-/-}$*Ptprf*$^{\Delta P/\Delta P}$ (**H**) CNDs. Scale bars: 10 μm. The results shown are means ± SEM. Ab (–), no primary antibody.

both control and *Ptprs*$^{-/-}$*Ptprf*$^{\Delta P/\Delta P}$ embryos at E12.5. For the executioner caspase-3, the results were consistent with the TUNEL assays, showing a moderate decrease in activated caspase-3–positive cells in the middle CND (from 33% to 22%, $P < 0.001$; Figure 4L) and a more prominent difference in the caudal CND of *Ptprs*$^{-/-}$*Ptprf*$^{\Delta P/\Delta P}$ compared with control embryos (46% to 23%, $P < 0.01$; Figure 4L). However, the extrinsic pathway–activated caspase-8 signals were uniform throughout the CND and did not display any significant difference between control and *Ptprs;Ptprf* double-mutant embryos (Figure 4M).

To exclude additional possibilities for the maintenance of the CND in *Ptprs*$^{-/-}$*Ptprf*$^{\Delta P/\Delta P}$ embryos, we determined the proliferation index in the CND and estimated tissue compaction (divergent retraction) by counting the number of cells per CND circumference. None of these parameters was found to be affected in *Ptprs*$^{-/-}$*Ptprf*$^{\Delta P/\Delta P}$ embryos (data not shown). Hence, we concluded that RPTPσ and LAR together play a crucial role in the process of distal ureter maturation by promoting CND apoptosis through the intrinsic apoptotic pathway.

RPTPσ interacts with Ret and modulates phosphorylation at pY1015/1062. Since the Ret receptor tyrosine kinase is involved in distal ureter maturation (12), it may well be among the potential molecular targets of RPTPσ and LAR. Importantly, LAR was previously shown to bind and modulate the phosphorylation and activity of an oncogenic variant of Ret (MEN2A), supporting the possibility of Ret being a direct substrate for RPTPσ and LAR (27). To assess whether RPTPσ can also interact with Ret, HEK293T cells were transfected with Ret and WT RPTPσ (RPTPσ-WT) expression vectors. To stabilize any putative interaction, an inactive substrate-trapping variant of RPTPσ with an Asp to Ala (D/A) mutation in the D1 phosphatase domain (RPTPσ-D/A) was cotransfected with Ret in a parallel experiment. Following transfection, cells were treated with GDNF/GFRα1 to activate Ret signaling. Interestingly, immunoprecipitation with an anti-RPTPσ antibody revealed a specific binding of Ret to RPTPσ-WT as well as RPTPσ-D/A proteins, independent of GDNF/GFRα1 stimulation (Figure 5A, lanes 5, 6, 11, and 12). In this assay, inclusion of the substrate-trapping D/A mutation did not significantly increase the interaction between

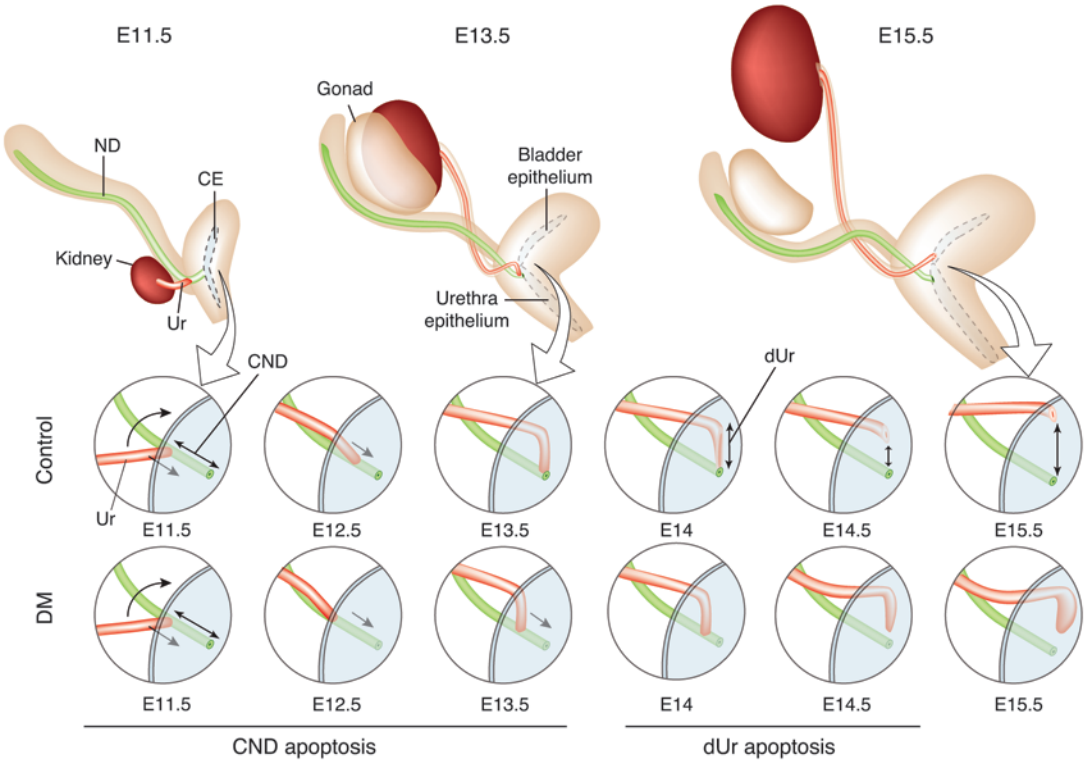

Figure 7
Model of distal ureter rearrangement. At E11.5, a segment of the nephric duct (green) that lies between the ureteric bud site (red) and the cloaca (blue) is defined as the CND. At E12.5, this structure undergoes apoptosis, which allows the descent of the distal end of the ureter toward the bladder epithelium. At E13.5–E14, the distal ureter has completely laid down against the bladder epithelium and undergoes apoptosis. This causes the separation of the ureter from the nephric duct. At E14.5, these 2 structures are now separated and the ureter forms an orifice in the bladder epithelium, while the nephric duct drains into the urethra. Subsequent growth of the bladder allows for further separation of the 2 orifices. In E12.5 *Ptprs;Ptprf* double-mutant embryos, the CND undergoes insufficient apoptosis to eliminate the structure in a timely fashion, thus affecting the process of distal ureter rearrangement. The initiation of urine production around E15.5–E16.5 pressures the distal end of the ureter, which leads to ureterocele formation.

Ret and RPTPσ. These results suggest that RPTPσ forms a complex with Ret even in the absence of GDNF stimulation. Next, we examined whether RPTPσ modulates GDNF/Ret downstream signaling. For this, Ret activation was estimated using phospho-specific antibodies against pY1015 and pY1062, which are key phospho-tyrosine docking sites for PLCγ and AKT/MAPK activation, respectively (29). The transfection of Ret together with RPTPσ-WT showed a decrease in the phosphorylation levels of Ret pY1015 and pY1062 in total cell lysates (Figure 5A, lanes 4, 5, 10, and 11). In line with this result, the phosphorylation levels of PLCγ, AKT, and ERK were also decreased in the presence of RPTPσ-WT. Furthermore, the RPTPσ-D/A trapping mutant also blocked the phosphorylation of the PLCγ and ERK pathways as well as the AKT pathway to a lesser extent (in Figure 5A, compare lanes 4 and 6 and lanes 10 and 12). Taken together, these data indicate that RPTPσ negatively regulates both the basal and GDNF-induced signaling downstream of Ret pY1015 and pY1062.

Ret suppresses RPTPσ-induced apoptosis. The phospho-tyrosines pY1015 and pY1062 in Ret have been implicated in its prosurvival activity (30), whereas for RPTPσ and LAR, several studies point to a proapoptotic effect (31–36). To further investigate whether Ret and RPTPσ may form a physiological dyad in apoptosis, we transfected HEK293 cells with RPTPσ and a Ret-GFP fusion protein or GFP alone as a control (Figure 5B). Early apoptotic cell death was measured by flow cytometry detecting annexin V–PE and 7-AAD on the GFP-positive cell fraction. Cotransfection of RPTPσ-WT together with GFP significantly increased the proportion of apoptotic GFP-positive cells (Figure 5B). In contrast, cotransfection of RPTPσ-WT with Ret-GFP completely abolished RPTPσ-driven apoptotic cell death. Taken together, these results suggest that the prosurvival activity of Ret can efficiently oppose the proapoptotic activity of LAR-RPTPs.

Ret (pY1015) is hyperphosphorylated in $Ptprs^{-/-}Ptprf^{\Delta P/\Delta P}$ *CND*. In order to further verify the activity of LAR-RPTPs on Ret phosphorylation, we performed immunostainings with antibodies against Ret (pY1015), Ret, and E-cadherin on histological sections of control and double-mutant mouse embryos. Although total Ret expression was not altered in $Ptprs^{-/-}Ptprf^{\Delta P/\Delta P}$ CNDs (Figure 6, D–F), the Ret (pY1015) signal was significantly stronger in $Ptprs^{-/-}Ptprf^{\Delta P/\Delta P}$ CNDs in comparison with control CNDs at E12.5 ($P < 0.005$) (Figure 6, A–C and F). E-cadherin staining, used as a control, was unaltered in these experiments (Figure 6F). Together, these data support the negative activity of LAR-RPTPs on Ret tyrosine phosphorylation.

To determine whether LAR-RPTPs additionally counteract Ret signaling at the transcriptional level, we examined Ret expression

in the CND of control and *Ptprs;Ptprf* double-mutant embryos. Interestingly, although Ret is expressed at E11.5 (data not shown), when CND elimination is initiated, its expression was significantly reduced in control embryos at E12.5 (Figure 6G). However, this transcriptional downregulation was not affected in *Ptprs;Ptprf* double-mutant embryos (Figure 6, G and H). Hence, the gradual downregulation of Ret expression in the CND may further facilitate the proapoptotic activity of LAR-RPTPs in that region but is, in itself, independent of LAR-RPTPs activity.

Discussion

Although LAR-RPTPs are expressed in several organs during mouse development (37), relatively few studies have addressed their developmental role. This is largely due to the close similarity between all 3 LAR-RPTP paralog genes, which results in functional redundancy at the cellular level. This has recently been demonstrated for the LAR-RPTPs RPTPσ and RPTPδ in motor axon targeting (18), a function that could not be identified in any of the single mutant phenotypes (19, 38). Among the embryonic structures in which the expression of LAR-RPTPs can be detected are components of the urogenital system, in which *Ptprs* and *Ptprf* are especially strongly expressed (37). To determine the role of these 2 phosphatases in the morphogenesis of the urogenital system and other tissues, we performed an allelic series using inactivation mutations for both genes in the mouse. This study revealed crucial roles for LAR-RPTPs in craniofacial morphogenesis and in distal ureter maturation.

The detailed analysis of the urinary tract phenotype showed that LAR-RPTPs are necessary for the apoptosis-mediated remodeling of the distal ureter. The characterization of this phenotype led us to focus on the sequence of events necessary for the repositioning of the ureter from its site of induction in the nephric duct to its final connection point within the bladder epithelium, a process requiring elimination of the CND by apoptosis (10). Our analysis not only confirms but also extends this observation, by revealing that CND removal allows a segment of the distal ureter to lay against the epithelium of the bladder primordium. This segment is subsequently also eliminated by apoptosis, which creates a new connection site for the ureter in the primordium region, giving rise to the bladder, while the nephric duct stays in contact with the epithelial region that will develop into the urethra (Figure 7). The elimination of a distal ureter segment in combination with the growth of the urethra/bladder primordium resolves the question of ureter and nephric duct separation. Importantly, this extended model of distal ureter maturation is also compatible with the classic model proposed by Mackie and Stephens (2), which states that an ectopic rostral ureter budding site would lead to VUJO. According to our model, such a rostral budding site would be too far from the cloaca epithelium to allow a complete elimination of the distal ureter by apoptosis. Conversely, an ectopic budding site in the caudal nephric duct would result in a ureter connection too high in the bladder, resulting in vesicoureteral reflux. We predict that this is caused by a premature lay down and death of the distal ureter, possibly associated with an incomplete rotation of the ureter around the nephric duct axis (Figure 7). A short movie depicting our model is presented as Supplemental Video 1.

The critical importance of apoptotic cell death for distal ureter maturation is confirmed by the *Ptprs;Ptprf* double-mutant mouse phenotype. These embryos harbor up to 80% reduction in the apoptotic index of CND cells, which leads to a considerable slow down in the ureter maturation process. Interestingly, the remaining apoptotic activity seems sufficient to create a threshold mechanism by which the ureter either is brought to the vicinity of the bladder region, thereby generating VUJO and ureterocele, or reaches the bladder region, leading to much milder phenotypical consequences such as dilated ureter. This threshold mechanism would reconcile the incomplete penetrance of the hydronephrosis/hydroureter phenotype at E18.5 given the 100% penetrance of the apoptotic phenotype prior to E15.5. Such a mechanism may also underlie the variability in urinary tract manifestations observed in CAKUT disease patients.

The activation of programmed cell death is a powerful means to perform morphogenetic rearrangements during embryogenesis. During vertebrate organogenesis, it has notably been observed in the formation of the digits, heart chambers, and inner ear (reviewed in ref. 39). Here we show that RPTPσ and LAR regulate apoptosis through caspase-3 activation but in a caspase-8–independent manner. This is interesting, since the steep apoptosis gradient that we and others (10) observed in the CND suggests that the apoptotic trigger comes from surrounding tissues, notably the cloaca epithelium. Although our results do not exclude such an extracellular activation of apoptosis, they argue against involvement of the caspase-8–dependent extrinsic pathway.

Our data additionally reveal an intricate relationship between LAR-RPTPs and the Ret receptor tyrosine kinase in the regulation of apoptotic cell death. Ret is known as a ligand-dependent prosurvival factor through its activation of PLCγ, Ras/MAPK, PI3K/AKT, and JNK pathways (13). On the other hand, LAR-RPTPs display clear proapoptotic potential along pathways that may involve p130CAS and DAPK (33–36). We and others (27) demonstrated that LAR-RPTPs interact with and modulate Ret tyrosine phosphorylation at critical tyrosine residues, resulting in the downregulation of the PLCγ, ERK, and AKT pathways. In addition, our results show that catalytically inactive RPTPσ-D/A mutants also downregulated Ret signaling, indicating that RPTPσ may not directly dephosphorylate Ret but rather act by preventing dimerization of the receptor, thus attenuating its tyrosine autophosphorylation. A similar mechanism was proposed for the regulation of Ret-MEN2A by LAR (27). Most importantly, our results demonstrate that Ret (pY1015) was significantly hyperphosphorylated in *Ptprs;Ptprf* double-mutant CNDs, where apoptotic cell death should take place under normal conditions. Together, these observations suggest a functional dyad in which LAR-RPTP proapoptotic and Ret prosurvival activities in the CND together determine the balance toward cell death. Interestingly, the RPTP-independent transcriptional downregulation of Ret that we observed in the maturing CND would thus further tip the balance toward the apoptotic response in these cells. It is also tempting to speculate that the negative regulation of Ret by LAR-RPTPs is already effective during the independent process of ureter budding, thereby providing an explanation for the 13% frequency of duplex systems that we observe in *Ptprs*$^{-/-}$*Ptprf*$^{\Delta P/\Delta P}$ embryos.

The occurrence of urinary tract defects in combination with craniofacial abnormalities in *Ptprs;Ptprf* double-mutant embryos is interesting. The malformations include a small lower jaw (micrognathia), cleft palate, exencephaly, and a number of milder manifestations. As these defects are characteristic of neural crest cell deficiencies during mid-stage embryogenesis, it is likely that LAR-RPTPs play a role in the normal colonization of the facial mesenchyme by neural crest cells. However, other malformations such as

those observed in the eye of *Ptprs;Ptprf* double-mutants may not be linked to the neural crest. It is interesting to note that several aspects of craniofacial development involve apoptosis-mediated morphogenesis. These include neural crest cell formation, palate fusion, and hyaloid artery elimination in the eye (40–42). It is therefore plausible that the role of LAR-RPTPs in these structures also involves a regulation of programmed cell death. A detailed analysis of the mechanisms underlying the craniofacial defects will be necessary to resolve these issues.

Noticeably, the penetrance of the craniofacial and urinary tract *Ptprs;Ptprf* double-mutant phenotypes was incomplete at E18.5. In addition, these phenotypes were not found to come in strict association. This suggests that alternative mechanisms can partially compensate for the lack of RPTPσ and LAR in these tissues. An obvious candidate for this function is the third member of the LAR-RPTP family, RPTPδ, which is expressed at low levels in the distal ureter as well as in the developing head (37). The incomplete penetrance of the *Ptprs;Ptprf* phenotypes is reminiscent of congenital disorders that affect different organ systems with variable phenotypic manifestations. Among these disorders is Hirschsprung disease (OMIM #142623) a disease mostly affecting the neural crest that has been associated with both urogenital and craniofacial malformations. Notably, Ret is one of the main causative genes associated with this disease (43). Another interesting condition is DiGeorge syndrome (microdeletion 22q11.2; OMIM #188400), which includes characteristic craniofacial, heart, and immune abnormalities as a result of a defect in cervical neural crest cell migration. Interestingly, DiGeorge syndrome is frequently found in association with renal agenesis, dysplasia, and hydronephrosis (44). Although the phenotype of *Ptprs;Ptprf* double-mutant embryos does not strictly overlap with these diseases, the association between craniofacial malformations and urinary tract defects is intriguing, as it suggests that LAR-RPTPs or one of their cellular targets may be mechanistically involved in congenital human syndromes.

Methods

Generation of RPTPσ;LAR double-mutant mice. Mutant mice lacking either RPTPσ or LAR phosphatase activity have been described previously (19, 23). These animals were backcrossed for at least 6 generations to C57BL/6J. Double-homozygous mutant mice were obtained by intercrossing double-heterozygous parents. Noon of the day of vaginal plug detection was considered E0.5. Mice were kept under pathogen-free conditions in an environmentally controlled room at the Animal Resource Centre of McGill University. All animal procedures were approved by the McGill Animal Care Committee and were conducted according to the Canadian Council of Animal Care ethical guidelines for animal experiments.

Histopathological and immunohistochemical analyses. Tissues were dissected and fixed in phosphate-buffered 10% formalin (Fisher Scientific) and embedded in paraffin according to standard procedures. Serial 6-μm paraffin sections were made and stained with H&E. Alternatively, tissues were fixed in 4% paraformaldehyde/PBS at 4°C overnight and cryosectioned at 12 or 15 μm for immunohistochemistry. The following primary antibodies were used: rabbit anti-Pax2 antibody (1:250; Covance), rat anti–E-cadherin (1:400; Zymed), rabbit anti-fibronectin (1:40; MD Biosciences), rabbit anti–cleaved caspase-3 (1:200; Cell Signaling Technology). Secondary detection was done using either anti-rabbit or anti-rat secondary antibodies labeled with Alexa Fluor 488 or Alexa Fluor 568 (1:200; Invitrogen). Caspase-8 histochemistry was done using Casp-GLOW Red Active Caspase-8 Staining Kit (1:300; Biovision). Sections for caspase-3 immunohistochemistry were processed with microwave antigen retrieval (5 mM EDTA, pH 8.0, 1 mM Tris, pH 7.5). Sections were occasionally counterstained with DAPI (50 mg/ml) (Invitrogen) in SlowFade Light mounting medium (Invitrogen). In these analyses, control embryos of different allelic combinations (not showing the phenotype) were used to compare with double knockout embryos.

In situ hybridizations. Embryos were prepared as for immunohistochemical staining. In situ hybridization with digoxigenin dUTP RNA probes was performed as described previously (45) using the following probes: *Ptprs* (20), *Ptprd* (46), *Ptprf* (37), and *Ret* (47).

Measurement of CND length. E11.5, E12.5, and E13.5 embryos were sectioned coronally, transversally, or sagittally and used for quantification of CND length. Length of CND was calculated as the hypotenuse according to the formula $c^2 = \sqrt{(a^2 + b^2)}$, where c indicates length of CND, a indicates length from ureter–nephric duct junction to the cloaca epithelium as measured by AxioVision digital image processing software (Zeiss), and b indicates section thickness multiplied by the number of sections between the ureter–nephric duct junction and the cloaca (urogenital sinus).

Quantification of apoptotic cells. TUNEL assay was performed on cryosections using the In Situ Cell Death Detection Kit (Roche) according to the manufacturer's instructions. TUNEL labeling was followed by anti-Pax2 antibody immunostaining, as described above. Apoptotic cells were counted only within Pax2-positive domains. CND sections were sorted into 3 groups: rostral CND (at the junction between nephric duct and ureter), middle CND, and caudal CND (closest to urogenital sinus). For caspase-8 and caspase-3 quantification, positive counts were determined within E-cadherin–positive domains. Cells were counted on the right and left CND separately.

Plasmids. The full-length murine *Ptprs* was cloned into pcDNA3.1$^+$ vectors (Invitrogen). The catalytically inactive mutant RPTPσ-D/A was generated by site-directed mutagenesis of D1516 into A in reference to Ptprs protein sequence NP_035348. The full-length *Ret* cDNA encoding the murine Ret-9 isoform was obtained from Invitrogen and cloned into the mammalian expression vector pcDNA3.1$^+$ (Invitrogen). Intracellular *Ret* fragment (aa 708–1,073) was amplified by PCR and cloned into GFP-containing pcDNA-DEST47 vectors (Invitrogen) according to the manufacturer's instructions.

Immunoprecipitation and Western blotting. The human renal epithelial cell line HEK293T was maintained in DMEM supplemented with 10% FBS. Cells were plated at approximately 90% confluency and plasmids were transiently transfected with Lipofectamine 2000 (Invitrogen) according to the manufacturer's instructions. Twenty-four hours after transfection, medium was replaced with DMEM/0.2% FBS for 2 hours and the cells were treated or not with GDNF 100 ng/ml (Promega) and 100 ng/ml GFRα1 (R&D Systems) for 10 min. Cells were rinsed on ice with PBS and lysed (50 mM HEPES [pH 7.5], 150 mM NaCl, 1.5 mM $MgCl_2$, 1 mM EGTA, 1% Triton X-100, 10% glycerol, 1 mM Na_3VO_4, 1 mM NaF, and Complete protease inhibitors [Roche]). Cell extracts were centrifuged at 16,000 *g* for 10 min at 4°C, and the protein concentration was calculated by a Bradford assay (Bio-Rad). Immunoprecipitations were performed with 3 mg of total cellular protein extracts using monoclonal antibodies 17G7.2 (raised against intracellular domain of RPTPσ) coupled to NHS-activated Sepharose beads (GE Healthcare). Western blot analysis was performed according to standard procedures using anti–Ret (C-19) (Santa Cruz Biotechnology Inc.), anti–Ret (pY1062) (Santa Cruz Biotechnology Inc.), and anti–Ret (pY1015) (Biosource; anti–c-Ret [pY1016 (human)]). Anti–phospho-ERK1/2 (Thr202/Tyr204), anti-ERK1/2, anti–phospho-PLCγ1 (Tyr783), anti-PLCγ1, anti–phospho-AKT (Ser473), and anti-AKT antibodies were obtained from Cell Signaling Technology.

Flow cytometry. HEK293T cells were transfected with plasmids as described above. Twenty-four hours after transfection, cells were washed with PBS and treated with 0.25% trypsin (EDTA free) (Invitrogen) for

10 min. Single-cell suspensions (10^6 cells) were incubated with Annexin V–PE and 7-AAD (Sigma-Aldrich) in binding buffer (10 mM HEPES, pH 7.4, 140 mM NaCl, 2.5 mM $CaCl_2$) according to the manufacturer's instructions. Cells were first gated on GFP-positive cells and then analyzed by flow cytometry for Annexin V–PE and 7-AAD staining. Data acquisition and analysis were done on FACScan flow cytometer (Becton Dickinson) using CellQuest software (BD Biosciences).

Quantification of immunofluorescent signals in the CND. Urogenital systems from E12.5 embryos were fixed in 10% buffered formalin and serially sectioned at a thickness of 12 μm on a cryostat. CND sections located between the ureter and cloaca epithelium were carefully selected for immunohistochemical analysis. Sections were washed with PBS and boiled in the antigen-retrieving buffer (10 mM sodium citrate, 0.05% Tween 20, pH 6.0) for 30 min. After 1 h of blocking (in PBS with 10% goat serum, 1% BSA [Cell Signaling Technology], 0.1% cold fish skin gelatin [Sigma-Aldrich], 0.1% Triton X-100, 0.05% Tween-20), sections were incubated with Ret (pY1015) (1:1,000), Ret (C-19) (1:500), and E-cadherin (1:400) primary antibodies overnight at 4°C. The secondary detection step was as described above in *Immunohistochemical analyses*. Fluorescent images were acquired without nonlinear editing, using Axiostar Plus (Zeiss). ImageJ software (NIH) was used to measure brightness values of right and left CNDs on each section, using an adjacent surface area identical in size for normalization.

The analysis was performed on a total of 4 CNDs per group (control and double mutant) and included a total of 18 to 24 sections per staining as follows: Ret (pY1015) (control, n = 18; $Ptprs^{-/-}Ptprf^{\Delta P/\Delta P}$, n = 18), Ret (control, n = 20; $Ptprs^{-/-}Ptprf^{\Delta P/\Delta P}$, n = 24), and E-cadherin (control, n = 18; $Ptprs^{-/-}Ptprf^{\Delta P/\Delta P}$, n = 18).

Statistics. Statistical analyses were performed as unpaired 2-tailed Student's t tests. Unless otherwise indicated in the figure legends, data are presented as mean ± SD. In all cases, P values of 0.05 or less were considered significant.

Acknowledgments

We thank Eva Mignon for her excellent help with animal care, as well as Marilene Paquet, Melina Narlis, and Marie-Helene Weech for their help with histopathological analysis. Thanks also to Bouchard's lab members for critical review of the manuscript. This work was supported by a grant from the Kidney Foundation of Canada to M. Bouchard and operating grants from the Canadian Institutes for Health Research to M. Bouchard and N. Uetani (MOP-84343) and to M.L. Tremblay (MOP-42482). M. Bouchard holds a Canada Research Chair in Developmental Genetics of the Urogenital System. M.L. Tremblay is a Jeanne and Jean-Louis Lévesque Chair in Cancer Research.

Received for publication August 19, 2008, and accepted in revised form January 21, 2009.

Address correspondence to: Maxime Bouchard, McGill University, McGill Cancer Pavilion, Room 415, 1160 Pine Avenue W, Montreal, Quebec H3A 1A3, Canada. Phone: (514) 398-3532; Fax: (514) 398-6769; E-mail: maxime.bouchard@mcgill.ca.

1. Daneman, A., and Alton, D.J. 1991. Radiographic manifestations of renal anomalies. *Radiol. Clin. North Am.* **29**:351–363.
2. Mackie, G.G., and Stephens, F.D. 1975. Duplex kidneys: a correlation of renal dysplasia with position of the ureteral orifice. *J. Urol.* **114**:274–280.
3. Miyazaki, Y., and Ichikawa, I. 2003. Ontogeny of congenital anomalies of the kidney and urinary tract, CAKUT. *Pediatr. Int.* **45**:598–604.
4. Thomas, J.C., DeMarco, R.T., and Pope, J.C., 4th. 2005. Molecular biology of ureteral bud and trigonal development. *Curr. Urol. Rep.* **6**:146–151.
5. Murawski, I.J., Myburgh, D.B., Favor, J., and Gupta, I.R. 2007. Vesico-ureteric reflux and urinary tract development in the Pax2 1Neu+/– mouse. *Am. J. Physiol. Renal Physiol.* **293**:F1736–F1745.
6. Grieshammer, U., et al. 2004. SLIT2-mediated ROBO2 signaling restricts kidney induction to a single site. *Dev. Cell.* **6**:709–717.
7. Kume, T., Deng, K., and Hogan, B.L. 2000. Murine forkhead/winged helix genes Foxc1 (Mf1) and Foxc2 (Mfh1) are required for the early organogenesis of the kidney and urinary tract. *Development.* **127**:1387–1395.
8. Miyazaki, Y., Oshima, K., Fogo, A., Hogan, B.L., and Ichikawa, I. 2000. Bone morphogenetic protein 4 regulates the budding site and elongation of the mouse ureter. *J. Clin. Invest.* **105**:863–873.
9. Basson, M.A., et al. 2005. Sprouty1 is a critical regulator of GDNF/RET-mediated kidney induction. *Dev. Cell.* **8**:229–239.
10. Batourina, E., et al. 2005. Apoptosis induced by vitamin A signaling is crucial for connecting the ureters to the bladder. *Nat. Genet.* **37**:1082–1089.
11. Costantini, F., and Shakya, R. 2006. GDNF/Ret signaling and the development of the kidney. *Bioessays.* **28**:117–127.
12. Batourina, E., et al. 2002. Distal ureter morphogenesis depends on epithelial cell remodeling mediated by vitamin A and Ret. *Nat. Genet.* **32**:109–115.
13. Asai, N., et al. 2006. RET receptor signaling: dysfunction in thyroid cancer and Hirschsprung's disease. *Pathol. Int.* **56**:164–172.
14. Jijiwa, M., et al. 2004. A targeting mutation of tyrosine 1062 in Ret causes a marked decrease of enteric neurons and renal hypoplasia. *Mol. Cell. Biol.* **24**:8026–8036.
15. Jain, S., Encinas, M., Johnson, E.M., Jr., and Milbrandt, J. 2006. Critical and distinct roles for key RET tyrosine docking sites in renal development. *Genes Dev.* **20**:321–333.
16. Wong, A., et al. 2005. Phosphotyrosine 1062 is critical for the in vivo activity of the Ret9 receptor tyrosine kinase isoform. *Mol. Cell. Biol.* **25**:9661–9673.
17. Pulido, R., Krueger, N.X., Serra-Pages, C., Saito, H., and Streuli, M. 1995. Molecular characterization of the human transmembrane protein-tyrosine phosphatase delta. Evidence for tissue-specific expression of alternative human transmembrane protein-tyrosine phosphatase delta isoforms. *J. Biol. Chem.* **270**:6722–6728.
18. Uetani, N., Chagnon, M.J., Kennedy, T.E., Iwakura, Y., and Tremblay, M.L. 2006. Mammalian motoneuron axon targeting requires receptor protein tyrosine phosphatases sigma and delta. *J. Neurosci.* **26**:5872–5880.
19. Elchebly, M., et al. 1999. Neuroendocrine dysplasia in mice lacking protein tyrosine phosphatase sigma. *Nat. Genet.* **21**:330–333.
20. Thompson, K.M., et al. 2003. Receptor protein tyrosine phosphatase sigma inhibits axonal regeneration and the rate of axon extension. *Mol. Cell. Neurosci.* **23**:681–692.
21. Sapieha, P.S., et al. 2005. Receptor protein tyrosine phosphatase sigma inhibits axon regrowth in the adult injured CNS. *Mol. Cell. Neurosci.* **28**:625–635.
22. Chagnon, M.J., et al. 2006. Altered glucose homeostasis in mice lacking the receptor protein tyrosine phosphatase sigma. *Can. J. Physiol. Pharmacol.* **84**:755–763.
23. Schaapveld, R.Q., et al. 1997. Impaired mammary gland development and function in mice lacking LAR receptor-like tyrosine phosphatase activity. *Dev. Biol.* **188**:134–146.
24. Van Lieshout, E.M., Van der Heijden, I., Hendriks, W.J., and Van der Zee, C.E. 2001. A decrease in size and number of basal forebrain cholinergic neurons is paralleled by diminished hippocampal cholinergic innervation in mice lacking leukocyte common antigen-related protein tyrosine phosphatase activity. *Neuroscience.* **102**:833–841.
25. Dunah, A.W., et al. 2005. LAR receptor protein tyrosine phosphatases in the development and maintenance of excitatory synapses. *Nat. Neurosci.* **8**:458–467.
26. Bernabeu, R., et al. 2006. Downregulation of the LAR protein tyrosine phosphatase receptor is associated with increased dentate gyrus neurogenesis and an increased number of granule cell layer neurons. *Mol. Cell. Neurosci.* **31**:723–738.
27. Qiao, S., et al. 2001. Differential effects of leukocyte common antigen-related protein on biochemical and biological activities of RET-MEN2A and RET-MEN2B mutant proteins. *J. Biol. Chem.* **276**:9460–9467.
28. Jin, Z., and El-Deiry, W.S. 2005. Overview of cell death signaling pathways. *Cancer Biol. Ther.* **4**:139–163.
29. Airaksinen, M.S., and Saarma, M. 2002. The GDNF family: signalling, biological functions and therapeutic value. *Nat Rev Neurosci* **3**:383–394.
30. Putzer, B.M., and Drosten, M. 2004. The RET proto-oncogene: a potential target for molecular cancer therapy. *Trends Mol. Med.* **10**:351–357.
31. MacKeigan, J.P., Murphy, L.O., and Blenis, J. 2005. Sensitized RNAi screen of human kinases and phosphatases identifies new regulators of apoptosis and chemoresistance. *Nat. Cell Biol.* **7**:591–600.
32. Weng, L.P., Yuan, J., and Yu, Q. 1998. Overexpression of the transmembrane tyrosine phosphatase LAR activates the caspase pathway and induces apoptosis. *Curr. Biol.* **8**:247–256.
33. Tisi, M.A., Xie, Y., Yeo, T.T., and Longo, F.M. 2000. Downregulation of LAR tyrosine phosphatase prevents apoptosis and augments NGF-induced neurite outgrowth. *J. Neurobiol.* **42**:477–486.
34. Weng, L.P., Wang, X., and Yu, Q. 1999. Transmembrane tyrosine phosphatase LAR induces apoptosis by dephosphorylating and destabilizing p130Cas. *Genes Cells.* **4**:185–196.
35. Wang, W.J., et al. 2007. The tumor suppressor

DAPK is reciprocally regulated by tyrosine kinase Src and phosphatase LAR. *Mol. Cell.* **27**:701–716.
36. Lorber, B., Hendriks, W.J., Van der Zee, C.E., Berry, M., and Logan, A. 2005. Effects of LAR and PTP-BL phosphatase deficiency on adult mouse retinal cells activated by lens injury. *Eur. J. Neurosci.* **21**:2375–2383.
37. Schaapveld , R.Q., et al. 1998. Developmental expression of the cell adhesion molecule-like protein tyrosine phosphatases LAR, RPTPdelta and RPTPsigma in the mouse. *Mech. Dev.* **77**:59–62.
38. Uetani, N., et al. 2000. Impaired learning with enhanced hippocampal long-term potentiation in PTPdelta-deficient mice. *EMBO J.* **19**:2775–2785.
39. Penaloza, C., Lin, L., Lockshin, R.A., and Zakeri, Z. 2006. Cell death in development: shaping the embryo. *Histochem. Cell Biol.* **126**:149–158.
40. Kulesa, P., Ellies, D.L., and Trainor, P.A. 2004. Comparative analysis of neural crest cell death, migration, and function during vertebrate embryogenesis. *Dev. Dyn.* **229**:14–29.
41. Dudas, M., Li, W.Y., Kim, J., Yang, A., and Kaartinen, V. 2007. Palatal fusion - where do the midline cells go? A review on cleft palate, a major human birth defect. *Acta Histochem.* **109**:1–14.
42. Hahn, P., et al. 2005. Persistent fetal ocular vasculature in mice deficient in bax and bak. *Arch. Ophthalmol.* **123**:797–802.
43. Amiel, J., et al. 2008. Hirschsprung disease, associated syndromes and genetics: a review. *J. Med. Genet.* **45**:1–14.
44. Kobrynski, L.J., and Sullivan, K.E. 2007. Velocardiofacial syndrome, DiGeorge syndrome: the chromosome 22q11.2 deletion syndromes. *Lancet.* **370**:1443–1452.
45. Henrique, D., et al. 1995. Expression of a Delta homologue in prospective neurons in the chick. *Nature.* **375**:787–790.
46. Mizuno, K., et al. 1993. MPTP delta, a putative murine homolog of HPTP delta, is expressed in specialized regions of the brain and in the B-cell lineage. *Mol. Cell. Biol.* **13**:5513–5523.
47. Pachnis, V., Mankoo, B., and Costantini, F. 1993. Expression of the c-ret proto-oncogene during mouse embryogenesis. *Development.* **119**:1005–1017.